

Dynamic layer rearrangement during growth of layered oxide films by molecular beam epitaxy

J.-H. Lee<sup>1,\*</sup>, G. Luo<sup>2,\*</sup>, I.C. Tung<sup>1,3</sup>, S.H. Chang<sup>4</sup>, Z. Luo<sup>4,5</sup>, M. Malshe<sup>6</sup>,  
M. Gadre<sup>2</sup>, A. Bhattacharya<sup>4,7</sup>, S. M. Nakhmanson<sup>8</sup>, J. A. Eastman<sup>4</sup>, H.  
Hong<sup>1</sup>, J. Jellinek<sup>6</sup>, D. Morgan<sup>2</sup>, D. D. Fong<sup>4</sup>, and J. W. Freeland<sup>1,+</sup>

<sup>1</sup>*X-ray Science Division, Argonne National Laboratory, Argonne, Illinois 60439, USA.*

<sup>2</sup>*Department of Materials Science & Engineering, University of Wisconsin-Madison, 1509 University Avenue, Madison, Wisconsin 53706, USA.*

<sup>3</sup>*Department of Materials Science and Engineering, Northwestern University, Evanston, Illinois 60208, USA.*

<sup>4</sup>*Materials Science Division, Argonne National Laboratory, Argonne, Illinois 60439, USA.*

<sup>5</sup>*National Synchrotron Radiation Laboratory, University of Science and Technology of China, Hefei, Anhui 230026, China.*

<sup>6</sup>*Chemical Sciences and Engineering Division, Argonne National Laboratory, Argonne, Illinois 60439, USA.*

<sup>7</sup>*Center for Nanoscale Materials, Argonne National Laboratory, Argonne, Illinois 60439, USA*

<sup>8</sup>*Department of Materials Science & Engineering, and Institute of Materials Science, University of Connecticut, Storrs, Connecticut 06269, USA*

<sup>+</sup> [freeland@anl.gov](mailto:freeland@anl.gov)

\* These authors contributed equally to this work.

The  $A_{n+1}B_nO_{3n+1}$  Ruddlesden-Popper (RP) homologous series offers a wide variety of functionalities including dielectric, ferroelectric, magnetic, and catalytic properties. Unfortunately, the synthesis of such layered oxides has been a major challenge due to the occurrence of growth defects that result in poor materials behavior in the higher order members. To understand the fundamental physics of layered oxide growth, we have developed an oxide molecular-beam epitaxy system with *in situ* synchrotron X-ray scattering capability. We present results demonstrating that layered oxide films can dynamically rearrange during growth, leading to structures that are highly unexpected based on the intended layer sequencing. Theoretical calculations indicate that rearrangement can occur in many layered oxide systems and suggest a general approach that may be essential for the construction of metastable RP phases. We demonstrate the utility of the newfound growth strategy by performing the first atomically controlled synthesis of single crystalline  $\text{La}_3\text{Ni}_2\text{O}_7$ .

The atomic-level synthesis of functional oxides and an understanding of their growth behavior provide opportunities to explore and control the intriguing properties of artificial layered oxide heterostructures<sup>1-3</sup>. Oxide molecular-beam epitaxy (MBE) has long been known to be a technique uniquely suited to the deposition of layered oxide materials that cannot be stabilized in bulk form<sup>4-6</sup>, as the shuttered deposition process permits the construction of a material atomic layer by atomic layer. However, the desire for high crystal quality requires sufficient adatom mobility to achieve the 2D growth mode, where each layer is completed before the next layer begins. With the elevated temperatures necessary for this mobility, other kinetic pathways (or other phases) may become competitive, and the resulting structure will be dictated by local thermodynamic and kinetic considerations<sup>7</sup>.

A longstanding challenge in the oxide thin film community has been the growth of (AO)(ABO<sub>3</sub>)<sub>n</sub> Ruddlesden-Popper (RP) compounds<sup>8</sup>, which consist of *n* unit cells of perovskite ABO<sub>3</sub> alternated with a layer of rocksalt AO along the crystallographic *c*-axis. As an illustration of the utility of oxide MBE for the synthesis of layered phases, Haeni *et al.*<sup>9</sup> grew the first five members of the (SrO)(SrTiO<sub>3</sub>)<sub>n</sub> homologous series (*n*=1 to 5), and Lee *et al.*<sup>10</sup> recently grew a structure with *n*=10. However, only a few members of the series are thermodynamically stable<sup>11-13</sup>. For this reason, as well as the high sensitivity of the material to the local Sr concentration, the resulting structures often exhibit intergrowth defects<sup>14-16</sup>. This highlights a clear need to quantitatively understand the interrelationships between the deposition process and naturally driven processes occurring within the growing crystal such that artificially layered structures can be more readily synthesized.

Here, we describe the results of a detailed study conducted on the initial growth of Sr<sub>2</sub>TiO<sub>4</sub> (*n*=1) on TiO<sub>2</sub>-terminated SrTiO<sub>3</sub> (001) substrates<sup>17</sup>, finding that the initial layers reconstruct through layer exchange into SrTiO<sub>3</sub> (*n* = ∞). The reaction can be understood from the energetics of different layer configurations determined with

computational theory, and insight from these calculations is used to form the  $\text{Sr}_2\text{TiO}_4$  phase directly by modification of the initial layering sequence. We then show the generality of the layer exchange phenomenon and demonstrate the utility of our growth strategy by stabilizing a new single-crystalline phase in the lanthanum nickelate system.

We employed a newly constructed oxide MBE system, built from an existing *in situ* X-ray chamber at Sector 33ID-E of the Advanced Photon Source (APS)<sup>18</sup>. The  $(\text{SrO})(\text{SrTiO}_3)_n$  films were grown at 750 °C and in  $10^{-6}$  Torr of  $\text{O}_2$  using a Sr effusion cell and a Ti-Ball<sup>TM</sup> source. Immediately following the shuttered deposition of each atomic layer, with the sequence  $\text{SrO} \rightarrow \text{SrO} \rightarrow \text{TiO}_2 \rightarrow \text{SrO}$ , we measured the scattered intensity under growth conditions along the out-of-plane direction (00L) at both non-resonant (15 keV) and resonant (at the Sr K-edge) X-ray energies. The X-ray results are shown in Fig. 1a, while the expected structure is shown in Fig. 1b. It can be readily observed that the intensity profile along the 00L, *i.e.*, the specular crystal truncation rod (CTR), for SrO #3 is virtually identical to that for SrO #2, which corresponds to the structure of a double SrO layer on the  $\text{SrTiO}_3$  substrate. If the CTR for SrO #3 represents the same structure, this suggests that the  $\text{TiO}_2$  has exchanged places with SrO #2, as depicted by the arrows in Fig. 1b. This interpretation was confirmed by quantitative fitting of the specular CTRs, revealing that the rearrangement happened either during or after growth of the  $\text{TiO}_2$  layer such that  $\text{SrO} \rightarrow \text{SrO} \rightarrow \text{TiO}_2$  deposition forms the SrO- $\text{TiO}_2$ -SrO structure. As seen from the time-evolution of scattered intensity at the highly surface sensitive anti-Bragg position (Supplementary information Fig. S1), changes are observed only with the Ti shutter open, providing evidence that the exchange occurred during  $\text{TiO}_2$  incorporation and is complete by the time 1 monolayer coverage of  $\text{TiO}_2$  is reached.

To understand the energetic driving force for this layer rearrangement, we calculated and compared the energies of different stacking sequences using density functional theory (DFT)<sup>19,20</sup> as well as with the empirical modified Buckingham potential (EP)<sup>21</sup>. We first compared two structures comprised of the

TiO<sub>2</sub>-terminated SrTiO<sub>3</sub> substrate with two SrO layers and one TiO<sub>2</sub> layer, as shown in Fig. 2a-b. Relative to the intended SrO-SrO-TiO<sub>2</sub> structure, the SrO-TiO<sub>2</sub>-SrO structure is more stable by 0.6 eV/Ti. This demonstrates that there is a significant thermodynamic driving force to rearrange the layers from SrO-SrO-TiO<sub>2</sub> to a SrO-TiO<sub>2</sub>-SrO structure, in agreement with the exchange observed in Fig. 1. The good agreement between the DFT and EP results shows that the physics captured by the EP, i.e., short-range bonding and electrostatics, dominates the exchange energetics.

We then considered the effect of a third consecutive SrO layer in the stacking sequence, as shown in Fig. 2c. The SrO-SrO-TiO<sub>2</sub>-SrO structure (Fig. 2d) was determined to be ~1 eV/Ti more stable than SrO-SrO-SrO-TiO<sub>2</sub> and ~0.4 eV/Ti more stable than SrO-TiO<sub>2</sub>-SrO-SrO (Fig. 2e). TiO<sub>2</sub> will then exchange with the topmost SrO layer but not with the layer underneath. This result suggests that the immediate growth of the RP phase can be accomplished by following the SrO→SrO→SrO→TiO<sub>2</sub> deposition sequence. We tested this hypothesis experimentally, again measuring the scattered intensity along the specular CTR after the growth of each layer. The final structure was SrO-SrO-TiO<sub>2</sub>-SrO, as predicted, and continued growth of Sr<sub>2</sub>TiO<sub>4</sub> can be accomplished by following the SrO→SrO →TiO<sub>2</sub> deposition sequence. Note that each TiO<sub>2</sub> layer will continue to exchange with the underlying SrO throughout the growth process, as the energetics for rearrangement change little as a function of film thickness (Supplementary information Fig. S2a). Thus, only one extra SrO layer in the initial sequence is needed to stabilize the proper sequencing for the RP phase.

While rearrangement of the initial SrO-SrO-TiO<sub>2</sub> structure is energetically favorable, the atomic pathway by which the configuration change occurs is less clear. One possible path is that Ti can move directly into the SrO layer, with the displaced SrO species presumably diffusing on top of the forming TiO<sub>2</sub> plane during deposition. Although direct insertion into a SrO layer by an isolated TiO<sub>2</sub> is a high energy process, with a 2.71 eV energy barrier, our DFT studies show that a TiO<sub>2</sub> molecule

on the SrO bilayer attracts two neighboring O atoms in the topmost SrO layer and forms a tetrahedral-like cluster, significantly disrupting the SrO layer and making it vulnerable to further attack (Supplementary information Fig. S3). With two nearby TiO<sub>2</sub> molecules, the disruption can reduce the energy barrier to 1.18 eV (Supplementary information Fig. S4), and in the presence of a Sr vacancy there is no barrier to TiO<sub>2</sub> incorporation, yielding a potentially rapid exchange process that can easily occur during the relatively slow TiO<sub>2</sub> deposition especially given the presence of step edges, islands, and defects that are connected to the synthesis of oxide thin films. Molecular dynamics (MD) simulations with partial coverage of TiO<sub>2</sub> show movement of Sr atoms close to the edge of the TiO<sub>2</sub> island from the underlayer to the surface, which is also consistent with role of defects as a pathway for layer swapping (Supplementary information Fig. S5). While the actual path that the system follows has not been observed directly, all of these mechanisms are consistent with our finding that the exchange is driven by TiO<sub>2</sub> layer deposition.

While the results presented so far have been specific to strontium titanate Ruddlesden-Popper structures and Sr<sub>2</sub>TiO<sub>4</sub> in particular, our calculations indicate that layer exchange is expected quite generally for different stoichiometries and materials systems. First, as shown in Fig. 3a, we illustrate that it is always energetically favorable for a TiO<sub>2</sub> surface layer to exchange with the underlying SrO layer without regard to the number of consecutive SrO layers. With this understanding, one can gain atomic level control over the growth any arbitrary (SrO)(SrTiO<sub>2</sub>)<sub>n</sub> RP sequence, as illustrated in Supplementary information Fig. S2b. Among stackings of (mSrO)TiO<sub>2</sub>(nSrO), for  $m+n > 2$ , the most stable configurations are the ones accompanied by at least two SrO planes underneath and at least one SrO plane above the TiO<sub>2</sub> (i.e.,  $m \geq 2$  and  $n \geq 1$ ). These energies are in accordance with the results of Fisher et al.<sup>22</sup>, who found that single TiO<sub>2</sub> planes surrounded by more than two consecutive SrO layers could be stabilized in a superlattice geometry even when the overall stoichiometry was not thermodynamically stable. Furthermore, we predict that layer rearrangement also occurs with other cations in the B-site, as shown in Fig. 3b. We considered seven

other perovskite-forming B-site cations: V, Mn, Zr, Mo, Ru, Rh, and Ir. These systems have cation radii ranging from ~67 to ~86 pm and different magnetic moments, but all show trends similar to those in the Ti system. Cations in the antiferromagnetic (AFM) and nonmagnetic (NM) states behaved similarly to those in the ferromagnetic (FM) state, suggesting that magnetism plays a minor role in driving the rearrangement (Supplementary information Fig. S6a-c).

Detailed analyses of the strontium titanate system reveal that the driving force for layer exchange can be understood in terms of the cleavage energies (e.g. energy to pull two surfaces apart) of three relevant interfaces, which are largely independent of surrounding environment. These interfaces are S/S, T/ST, and T/SS, where S, T, and “/” represent the SrO plane, the TiO<sub>2</sub> plane, and the interface, respectively. As elucidated in the Supplementary Information, the energy differences of different stackings can be quantitatively modeled by cleavage energy differences (Supplementary Information Fig. S7). The cleavage energies of the three interfaces are ordered as S/S (~1.34 eV) < T/ST (~2.17 eV) < T/SS (~2.62 eV). This ordering is intuitive: the S/S interface is less stable than the T/ST interface because it contains fewer chemical bonds per unit area, while the T/SS interface is more stable than that for T/ST, due to weaker bonding in the adjacent SS bilayer. Such energy ordering drives layer rearrangement in order to form more locally stable interfaces in place of less stable ones. Using the above-mentioned three cleavage energies in our model, we can accurately reproduce the DFT results in Fig. 3a, as shown in Supplementary Information Fig. S8.

Finally, we considered whether layer rearrangement is unique to strontium-based systems or can take place in other materials grown on SrTiO<sub>3</sub>, such as the lanthanum-based transition metal oxides, La<sub>n+1</sub>B<sub>n</sub>O<sub>3n+1</sub>. The La-based materials differ substantially from those of the strontium-based oxides in that the (001) planes are nominally polar<sup>23</sup>, in contrast to the mostly charge neutral planes in strontium systems. As observed in Fig. 3c, layer rearrangement is again expected to occur for many B-site cations. The exchange will always take place on LaO trilayers,

regardless of the magnetic state. We do find, however, that the LaO-LaO-Mn and LaO-LaO-Fe structures are stable, whenever Mn or Fe are in the FM or AFM state, which may originate from large magnetic interactions (see Supplementary Information Fig. S6d-f).

To illustrate how our insight can provide a pathway to stabilize new phases and to confirm our predictions, we conducted a set of *in situ* growth experiments for  $(\text{LaO})(\text{LaNiO}_3)_n$  similar to those for the strontium titanates. We used a growth temperature of 600 °C and employed ozone as the oxidant. As predicted in Fig. 3c, layer rearrangement was indeed observed, and the same strategy for producing  $\text{Sr}_2\text{TiO}_4$  was used to grow both  $\text{La}_2\text{NiO}_4$  and  $\text{La}_3\text{Ni}_2\text{O}_7$ . The  $\text{La}_3\text{Ni}_2\text{O}_7$  structure was obtained by following the deposition sequence  $\text{LaO} \rightarrow \text{LaO} \rightarrow \text{LaO} \rightarrow \text{NiO}_2 \rightarrow \text{NiO}_2$ , which, after the predicted layer exchange, results in LaO-LaO-NiO<sub>2</sub>-LaO-NiO<sub>2</sub> ordering. Note that by combining the shuttered growth technique with this strategy, one achieves a level of control over cation ordering greater than that of direct transfer from stoichiometric target.<sup>24</sup> The specular CTR from a film grown by six repeats of that sequence is shown as the red curve in Fig. 4a, and its corresponding x-ray absorption spectroscopy (XAS) profile measured at the Ni *L*-edge is displayed in Fig. 4b. The specular CTR exhibits strong thickness fringes and Bragg peaks, indicating sharp interfaces and high crystalline quality. For comparison, a sample grown with the  $\text{LaO} \rightarrow \text{LaO} \rightarrow \text{NiO}_2 \rightarrow \text{LaO} \rightarrow \text{NiO}_2$  sequence is shown in black. There are no signs of the  $\text{La}_3\text{Ni}_2\text{O}_7$  Bragg peaks, and the scattered intensity exhibits signatures of a highly defective film. The XAS spectrum in Fig. 4b is compared with that from a  $\text{La}_3\text{Ni}_2\text{O}_{7-\delta}$  powder, where  $\delta$  is  $0 \pm 0.02$ , as determined by thermogravimetric analysis, illustrating that the nickel valence has the expected value of  $\sim 2.5+$ .

The synthesis methodology used here, coupling quantitative *in situ* X-ray scattering with computational theory, is an approach that can be readily extended to other layered materials and heterostructures. Of particular interest are those predicted to exhibit novel properties but have yet to be synthesized due to various growth

challenges, such as the polar  $\text{PbSr}_2\text{Ti}_2\text{O}_7$ <sup>25</sup> or many of the layered oxides described in Refs.<sup>26-29</sup>. One is not limited to simply layered oxides and can use this approach to explore wholly new oxide archetypes that have yet to be synthesized as thin film heterostructures. We find that the insights garnered when *in situ* X-ray results are fed back to computational theory to be of considerable importance as they allow the rapid formulation of growth strategies that may be critical to the material, even for deposition techniques as precise as MBE. This close integration with computational theory is an aspect of synthesis science that will become more essential as we create new materials by design and rapidly seek pathways to stabilize new phases.

## METHODS

Films were grown in the in-situ X-ray chamber at Sector 33ID-E of the Advanced Photon Source (APS) using molecular beam epitaxy. The  $(\text{SrO})(\text{SrTiO}_3)_n$  films were grown at 750 °C and in  $10^{-6}$  Torr of  $\text{O}_2$  using a Sr effusion cell and a Ti-Ball<sup>TM</sup> source. Grow rates ranged from 1-3 minutes per monolayer depending on the species.

We performed *ab initio* calculations using density functional theory (DFT), as coded in the Vienna *ab initio* simulation package (VASP)<sup>19,20</sup>. We chose the PBEsol functional<sup>30</sup>, which was demonstrated to be excellent for the description of bulk  $\text{SrTiO}_3$ <sup>31</sup>. The projector augmented wave (PAW) method is used with the following potentials for  $\text{SrTiO}_3$ : O ( $2s^2 2p^4$ , Ecut = 400.0 eV), Ti ( $3p^6 3d^{10} 4s^2$ , Ecut = 274.6 eV), and Sr ( $4s^2 4p^6 5s^2$ , Ecut = 229.3 eV). The plane-wave energy cutoff is set to 500 eV. We approximate the substrate with 20 atomic layers ( $\sim 3.7$  nm) of cubic  $\text{SrTiO}_3$ , with the bottom 10 atomic layers fixed to the optimized bulk positions and the other layers relaxed. To reduce the mirror interactions between neighboring supercells, we add a vacuum slab as thick as 1.5 nm and consider dipole corrections in the out-of-plane direction. The supercell in the plane are one or two unit cell sizes large and the Monkhorst-Pack k-point grids for Brillouin zone sampling are  $6 \times 6 \times 1$  and  $4 \times 4 \times 1$ , respectively.

The functional form and parameters of the empirical Buckingham potential<sup>21</sup> used in

structural optimizations and MD simulations are given in the Supplementary Information. The optimizations are performed using gradient-based techniques. The convergence criteria for energy and interatomic distances are 0.001 eV and 0.0005 Å, respectively. The MD runs are carried out with the Verlet propagator and a step size of 5 fs. A Nosé type thermostat, as implemented in the DL\_POLY software package, is used to control the temperature.

### Acknowledgements

The authors acknowledge discussions with D.G. Schlom, K. Lee, and Y. Nie, and support at the APS with H. Zhou and C. Schlepütz. S.H.C., J.A.E., A.B., and D.D.F. were supported by the U.S. Department of Energy, Office of Science, Materials Sciences and Engineering Division. Work performed at Argonne National Laboratory, including the Advanced Photon Source, was supported by the DOE, Basic Energy Sciences, under Contract No. DE-AC02-06CH11357. The calculations were carried out on the Fusion Cluster of Argonne's Laboratory Computing Resource Center, at NERSC (supported by DOE), and on Argonne's Carbon Cluster under award CNM29783 and CNM35702. D.M. and G.L. were partially supported by University of Wisconsin Materials Research Science and Engineering Center (DMR-1121288).

### Author contributions

J.H.L., Z.L., I.C.T., S.H.C., A.B., J.A.E., H.H., D.D.F., and J.W.F. developed the in-situ oxide MBE system and participated in the real time growth experiments. J.H.L., Z.L., I.C.T., D.D.F., and J.W.F. handled analysis of the experimental data. G.L., M.M., M.G., S.N., J.J., and D.M. were responsible for the detailed theoretical calculations related to the experiments. All authors participated in the discussion of data/analysis/conclusions and in the writing of the manuscript.

### Additional information

Supplementary information is available in the online version of the paper. Reprints

and permissions information is available online at [www.nature.com/reprints](http://www.nature.com/reprints).  
Correspondence and requests for materials should be addressed to D.M. or J.W.F.

#### Competing financial interests

The authors declare no competing financial interests.

FIGURES

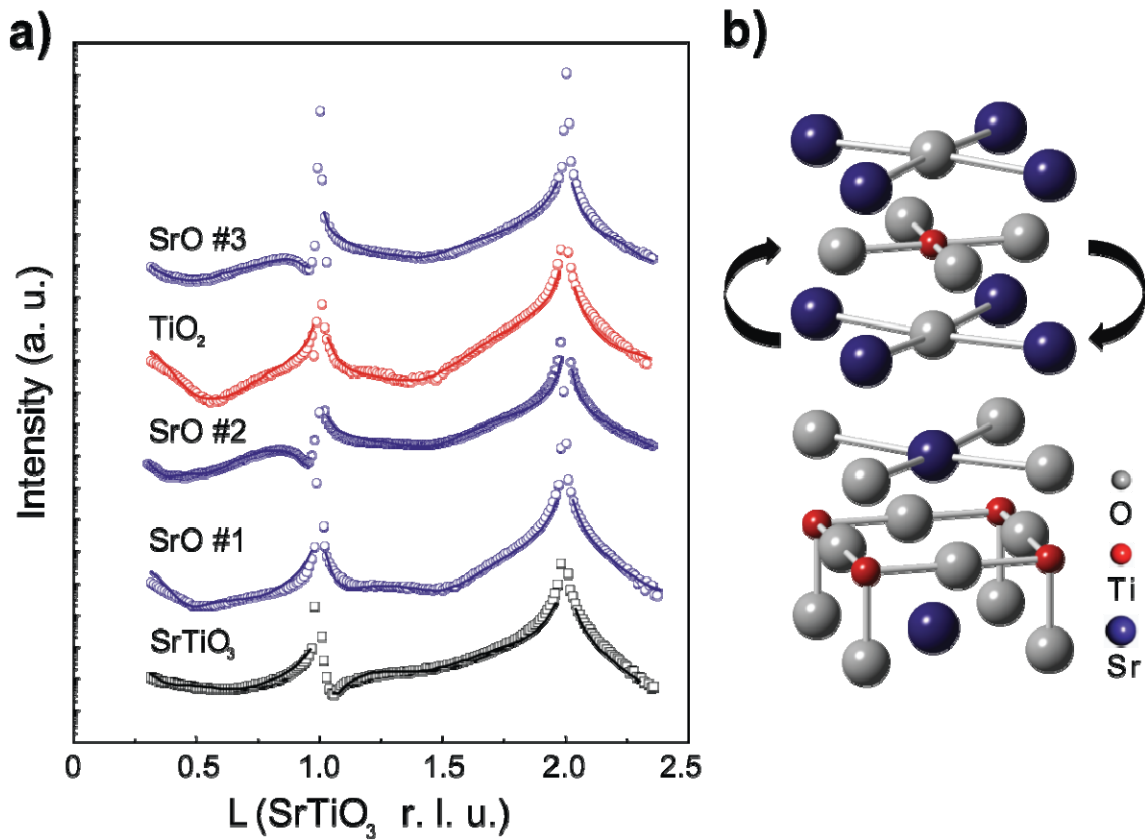


**Figure 1 | Layer swap during the growth of  $\text{Sr}_2\text{TiO}_4$ .** **a**, Scattered intensities along the 00L measured immediately after shuttered growth of each layer in the following sequence:  $\text{SrO} \rightarrow \text{SrO} \rightarrow \text{TiO}_2 \rightarrow \text{SrO}$  (from bottom to top). The measured data are represented by symbols, and fitted intensities are represented by solid lines. **b**, The expected atomic structure of film based on the growth sequence and proposed layer swap which occurs in the real growth.

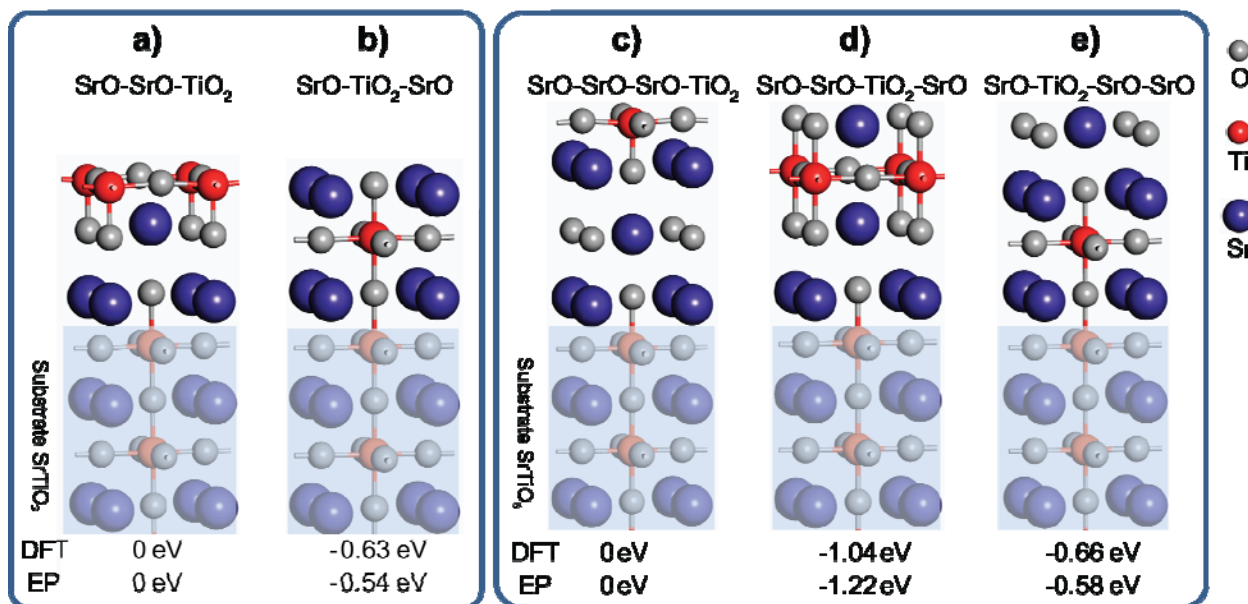


**Figure 2 | Energetics for different layer sequencing during growth.** Optimized structures and relative energies of different stackings of two or three SrO and one TiO<sub>2</sub> layers on a TiO<sub>2</sub> terminated SrTiO<sub>3</sub> substrate. Stackings are labeled by their layers from the first layer above the substrate surface to the top interface with vacuum. All relative energies are measured per unit cell and have the unit of eV per exchanged Ti. Part of the substrate is indicated by shaded areas to guide the eyes. DFT = density functional theory and EP = empirical potential.

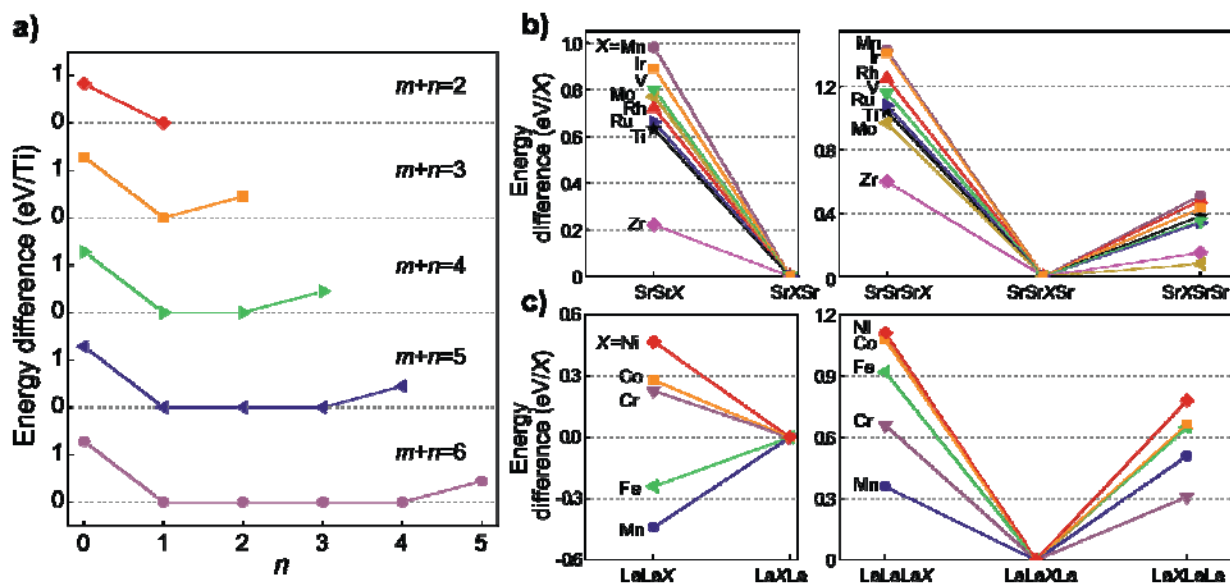


**Figure 3 | Layer swapping in additional systems.** **a**, Energy differences among stackings of (TiO<sub>2</sub>-terminated substrate)-(mSrO)TiO<sub>2</sub>(nSrO) for  $m + n = 2, 3, 4, 5, 6$ . For simple stacking notation, hereafter, we leave out the substrate and the O in an oxide layer. Thus, the (TiO<sub>2</sub>-terminated substrate)-(mSrO)TiO<sub>2</sub>(nSrO) is written as (mSr)Ti(nSr). **b**, Energy differences among stackings of (mSr)X(nSr) at  $m + n = 2$  and 3 for X=Ti, V, Mn, Zr, Mo, Ru, Rh, and Ir in the B-site. **c**, Energy differences among stackings of (mLa)X(nLa) at  $m + n = 2$  and 3 for X=Cr, Mn, Fe, Co, and Ni in the B-site. All calculations for magnetic systems are done with ferromagnetic (FM) ordering.

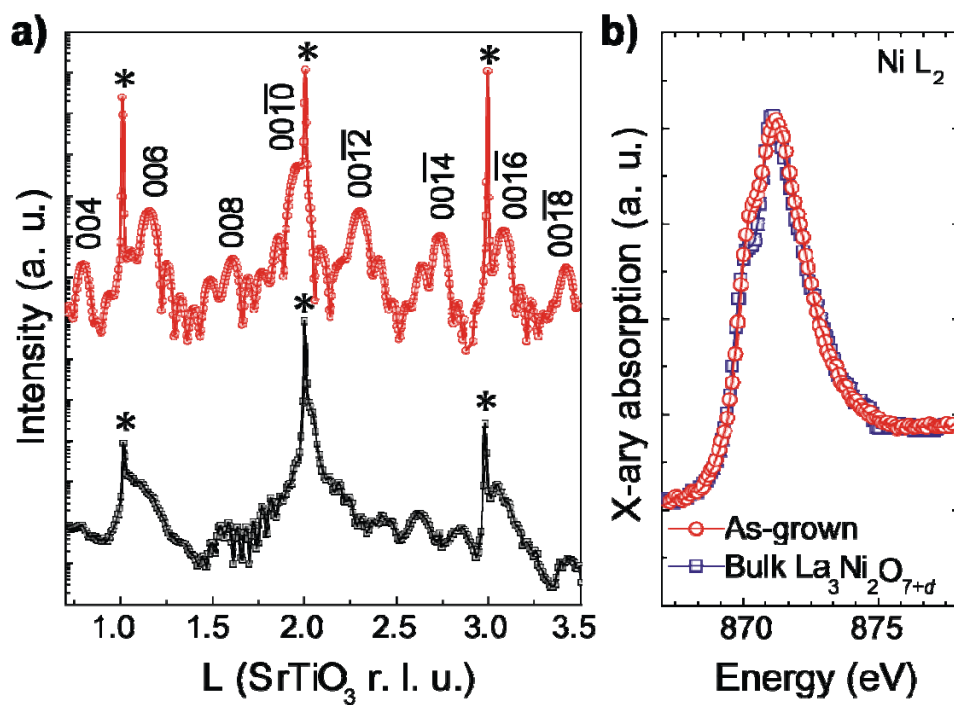


**Figure 4 | Synthesis of single crystal  $\text{La}_3\text{Ni}_2\text{O}_7$ .** **a**, Specular CTRs for a film grown with the  $\text{LaO} \rightarrow \text{LaO} \rightarrow \text{LaO} \rightarrow \text{NiO}_2 \rightarrow \text{NiO}_2$  sequence (red) and for film grown using the  $\text{LaO} \rightarrow \text{LaO} \rightarrow \text{NiO}_2 \rightarrow \text{LaO} \rightarrow \text{NiO}_2$  sequence (black). Peaks from the substrate are indicated with asterisks. **b**, XAS spectra for the  $\text{La}_3\text{Ni}_2\text{O}_7$  film (red) and a powder sample (blue).

1. Bibes, M., Villegas, J. & Barthelemy, A. Ultrathin oxide films and interfaces for electronics and spintronics. *Adv. Phys.* **60**, 5–84 (2011).
2. Chakhalian, J., Millis, A. J. & Rondinelli, J. Whither the oxide interface. *Nat. Mater.* **11**, 92–94 (2012).
3. Rondinelli, J. M., May, S. J. & Freeland, J. W. Control of octahedral connectivity in perovskite oxide heterostructures: An emerging route to multifunctional materials discovery. *MRS Bull.* **37**, 261–270 (2012).
4. Eckstein, J. N. & Bozovic, I. High-temperature superconducting multilayers and heterostructures grown by atomic layer-by-layer molecular beam epitaxy. *Annu. Rev. Mater. Sci.* **25**, 679–709 (1995).
5. Yamamoto, H., Naito, M. & Sato, H. A new superconducting cuprate prepared by low-temperature thin-film synthesis in a Ba-Cu-O system. *Jpn. J. Appl. Phys.* **36**, L341–L344 (1997).
6. Schlom, D. G., Chen, L.-Q., Pan, X., Schmehl, A. & Zurbuchen, M. A. A Thin Film Approach to Engineering Functionality into Oxides. *J. Am. Ceram. Soc.* **91**, 2429–2454 (2008).
7. Locquet, J.P., Catana, A., Mächler, E., Gerber, J. & Bednorz, J.G. Block-by-block deposition: A new growth method for complex oxide thin films. *Appl. Phys. Lett.* **64**, 372–374 (1994).
8. Ruddlesden, S. N. & Popper, P. New compounds of the  $K_2NiF_4$  type. *Acta Cryst.* **10**, 538–539 (1957).
9. Haeni, J. H. *et al.* Epitaxial growth of the first five members of the  $Sr_{n+1}Ti_nO_{3n+1}$  Ruddlesden–Popper homologous series. *Appl. Phys. Lett.* **78**, 3292 (2001).
10. Lee, C.-H. *et al.* Effect of reduced dimensionality on the optical band gap of  $SrTiO_3$ . *Appl. Phys. Lett.* **102**, 122901 (2013).
11. Udayakumar, K. R. & Cormack, A. N. Structural Aspects of Phase Equilibria in the Strontium-Titanium-Oxygen System. *J. Am. Ceram. Soc.* **71**, C469–C471 (1988).
12. Noguera, C. Theoretical investigation of the Ruddlesden-Popper compounds  $Sr_{n+1}Ti_nO_{3n+1}$  ( $n=1-3$ ). *Phil. Mag. Lett.* **80**, 173–180 (2000).
13. Le Bacq, O., Salinas, E., Pisch, A., Bernard, C. & Pasturel, A. First-principles structural stability in the strontium–titanium–oxygen system. *Philos. Mag.* **86**, 2283–2292 (2006).
14. McCoy, M. A., Grimes, R. W. & Lee, W. E. Phase stability and interfacial structures in the  $SrO$ – $SrTiO_3$  system. *Philos. Mag. A* **75**, 833–846 (1997).
15. Tian, W., Pan, X. Q., Haeni, J. H. & Schlom, D. G. Transmission electron microscopy study of  $n= 1-5$   $Sr_{n+1}Ti_nO_{3n+1}$  epitaxial thin films. *J. Mater. Res.* **16**, 2013–2026 (2001).
16. Lee, C.-H. *et al.* Exploiting dimensionality and defect mitigation to create tunable microwave dielectrics. *Nature* **502**, 532–536 (2014).
17. Koster, G., Kropman, B. L., Rijnders, G. J. H. M., Blank, D. H. A. & Rogalla, H. Quasi-ideal strontium titanate crystal surfaces through formation of strontium hydroxide. *Appl. Phys. Lett.* **73**, 2920–2922 (1998).
18. Hong, H. & Chiang, T.-C. A six-circle diffractometer system for synchrotron X-ray studies of surfaces and thin film growth by molecular beam epitaxy. *Nucl.*

- Instr. Meth. Phys. Res. A* **572**, 942–947 (2007).
19. Kresse, G. & Furthmüller, J. Efficient iterative schemes for ab initio total-energy calculations using a plane-wave basis set. *Phys. Rev. B* **54**, 11169 (1996).
  20. Kresse, G. & Furthmüller, J. Efficiency of ab-initio total energy calculations for metals and semiconductors using a plane-wave basis set. *Comp. Mater. Sci.* **6**, 15–50 (1996).
  21. Sekiguchi, S. *et al.* Atomic force microscopic observation of SrTiO<sub>3</sub> polar surface. *Solid State Ionics* **108**, 73–79 (1998).
  22. Fisher, P. *et al.* A series of layered intergrowth phases grown by molecular beam epitaxy: Sr<sub>m</sub>TiO<sub>2+m</sub> (m=1–5). *Appl. Phys. Lett.* **91**, 252901 (2007).
  23. Goniakowski, J., Finocchi, F. & Noguera, C. Polarity of oxide surfaces and nanostructures. *Rep. Prog. Phys.* **71**, 016501 (2008).
  24. Wu, K.-T., Soh, Y.-A., Skinner, S. J., Epitaxial growth of mixed conducting layered Ruddlesden–Popper La<sub>n+1</sub>Ni<sub>n</sub>O<sub>3n+1</sub> (n = 1, 2 and 3) phases by pulsed laser deposition, *Mater. Res. Bull.* **48**, 3783 (2013).
  25. Nakhmanson, S. M. & Naumov, I. Goldstone-like States in a Layered Perovskite with Frustrated Polarization: A First-Principles Investigation of PbSr<sub>2</sub>Ti<sub>2</sub>O<sub>7</sub>. *Phys. Rev. Lett.* **104**, 097601 (2010).
  26. Benedek, N. & Fennie, C. Hybrid Improper Ferroelectricity: A Mechanism for Controllable Polarization-Magnetization Coupling. *Phys. Rev. Lett.* **106**, (2011).
  27. Birol, T., Benedek, N. A. & Fennie, C. J. Interface Control of Emergent Ferroic Order in Ruddlesden–Popper Sr<sub>n+1</sub>Ti<sub>n</sub>O<sub>3n+1</sub>. *Phys. Rev. Lett.* **107**, 257602 (2011).
  28. Rondinelli, J. M. & Fennie, C. J. Octahedral Rotation-Induced Ferroelectricity in Cation Ordered Perovskites. *Adv. Mater.* **24**, 1961–1968 (2012).
  29. Mulder, A. T., Benedek, N. A., Rondinelli, J. M. & Fennie, C. J. Turning ABO<sub>3</sub> Antiferroelectrics into Ferroelectrics: Design Rules for Practical Rotation-Driven Ferroelectricity in Double Perovskites and A<sub>3</sub>B<sub>2</sub>O<sub>7</sub>Ruddlesden–Popper Compounds. *Adv. Funct. Mater.* **23**, 4810–4820 (2013).
  30. Perdew, J. *et al.* Restoring the Density-Gradient Expansion for Exchange in Solids and Surfaces. *Phys. Rev. Lett.* **100**, 136406 (2008).
  31. Wahl, R., Vogtenhuber, D. & Kresse, G. SrTiO<sub>3</sub> and BaTiO<sub>3</sub> revisited using the projector augmented wave method: Performance of hybrid and semilocal functionals. *Phys. Rev. B* **78**, 104116 (2008).

## Supplementary Information for “Dynamic layer rearrangement during growth of layered oxide films by molecular beam epitaxy”

J.-H. Lee\*, G. Luo\*, I.-C. Tung, S.-H. Chang, Z. Luo, M. Malshe, M. Gadre, A. Bhattacharya, S. M. Nakhmanson, J. A. Eastman, H. Hong, J. Jellinek, D. Morgan, D. D. Fong, and J. W. Freeland

### **Time evolution of scattered intensity during growth**

During shuttered growth of our films, we monitor the scattered intensity at the (0 0 1/2) position (in reciprocal lattice units of SrTiO<sub>3</sub>). This "anti-Bragg" position is midway between the substrate and film Bragg peaks and is thus highly sensitive to surface roughness [Robinson & Tweet, Rep. Prog. Phys. **55**, 599 (1992)]. The time evolution shown in Fig. S1 takes place after the deposition of two consecutive SrO layers and during the shuttered growth of TiO<sub>2</sub>. We employed a Pilatus detector [Dectris®], which allows the specification of regions of interest for both the signal and the background. The opening and closing of the shutter for the Ti-Ball™ are indicated with arrows. As seen, no evolution in surface roughness takes place before the opening of the shutter or after the closing of the shutter, implying that layer exchange occurs during TiO<sub>2</sub> growth.

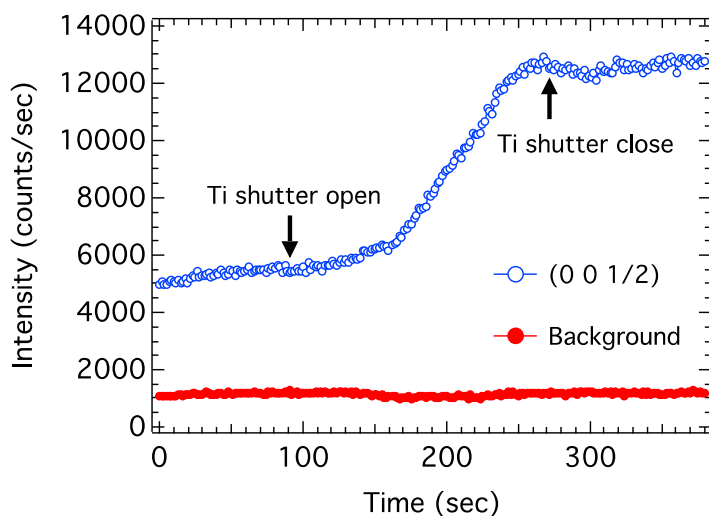


**Figure S1 | Time evolution of the scattered intensity at the (0 0 1/2) position during  $\text{TiO}_2$  layer deposition on a SrO bilayer.** Intensities from the both the signal (blue curve) and background (red curve) regions of interest are shown.

### **Deposition order for the growth of $\text{Sr}_2\text{TiO}_4$ and $(\text{SrO})_m(\text{SrTiO}_3)_n$ films on $\text{SrTiO}_3(001)$**

When the atomic layers  $\text{SrO} \rightarrow \text{SrO} \rightarrow \text{SrO} \rightarrow \text{TiO}_2$  are deposited on the  $\text{TiO}_2$ -terminated  $\text{SrTiO}_3(001)$  substrate, one unit cell of  $\text{Sr}_2\text{TiO}_4$  capped with an extra SrO layer ( $\text{SrO-SrO-TiO}_2\text{-SrO}$ ) are grown because of the layer swapping, as shown in Fig. S2a (upper). When the atomic layers  $\text{SrO} \rightarrow \text{SrO} \rightarrow \text{TiO}_2$  are deposited subsequently, the situation is similar to the deposition of  $\text{SrO} \rightarrow \text{SrO} \rightarrow \text{SrO} \rightarrow \text{TiO}_2$  considering the SrO layer capping. Figure S2a (lower) illustrates that the layer swapping continues and the second unit cell of  $\text{Sr}_2\text{TiO}_4$  is grown capped with a SrO layer. Further growth of  $\text{Sr}_2\text{TiO}_4$  films can be realized by continuing depositing atomic layers  $\text{SrO} \rightarrow \text{SrO} \rightarrow \text{TiO}_2$ .

Such strategy can be easily generalized to the growth of  $(\text{SrO})_m(\text{SrTiO}_3)_n$  film, as shown in Fig. S2b. According to Fig. 3a, deposited  $\text{TiO}_2$  on  $(\text{SrO})_{m+1}$  always has a driving force to swap with the top SrO layer, after which kinetic limitations and almost zero energy gains are expected to stop the swapping, thereby forming  $(\text{SrO})_m(\text{TiO}_2)(\text{SrO})$ . To obtain the correct stacking of the first unit cell, one needs to deposit  $(\text{SrO})_{m+1}(\text{SrTiO}_3)_n$ , which ends up with the stacking of

$(\text{SrO})_m(\text{SrTiO}_3)_n(\text{SrO})$  because of the swapping. To obtain a subsequent unit cell, one needs to deposit  $(\text{SrO})_m(\text{SrTiO}_3)_n$  because of the existing SrO layer.

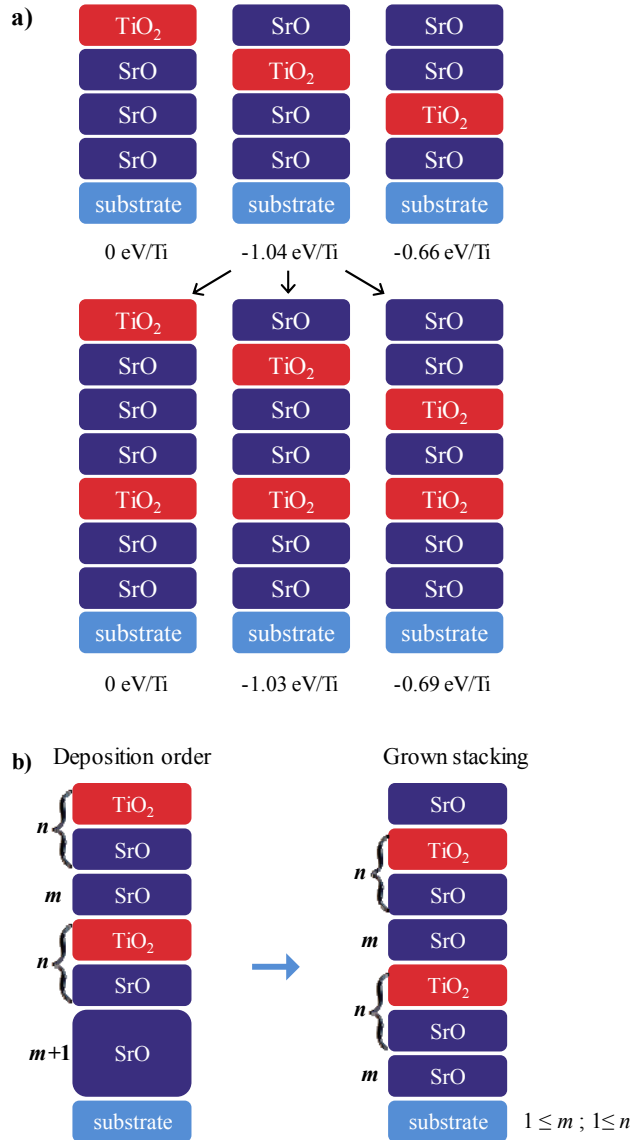


**Figure S2 | Strategy to grow  $\text{Sr}_2\text{TiO}_4$  and  $(\text{SrO})_m(\text{SrTiO}_3)_n$ .** **a**, Energy differences among different stackings in the growth of  $\text{Sr}_2\text{TiO}_4$  films. (upper) Different possible stackings after the deposition of  $\text{SrO} \rightarrow \text{SrO} \rightarrow \text{SrO} \rightarrow \text{TiO}_2$ ; (lower) Different possible stackings after the subsequent deposition of  $\text{SrO} \rightarrow \text{SrO} \rightarrow \text{TiO}_2$ . The relative energy of each stacking is labeled at the bottom. **b**, Illustration of the relationship between deposition order and the actual grown stacking for the first two unit cells of  $(\text{SrO})_m(\text{SrTiO}_3)_n$  film.

### Structure of SrO bilayer with one absorbing TiO<sub>2</sub> molecule

Figure S3 shows the structure of a TiO<sub>2</sub> molecule absorbing on the SrO bilayer. The Ti atom of the molecule attracts two O atoms in the topmost SrO layer and forms a tetrahedral-like TiO<sub>4</sub> molecule. The topmost SrO layer is thus greatly distorted and a large hole around one O site of the SrO layer is created, similar as introducing an O vacancy in the plane.

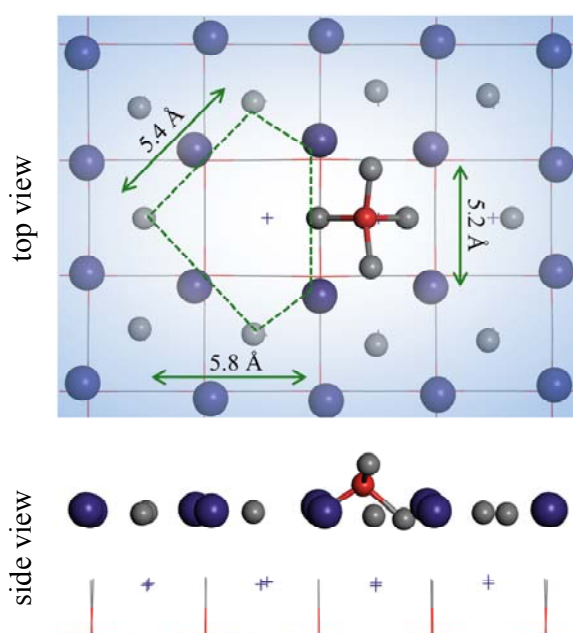


**Figure S3 | Structure of a TiO<sub>2</sub> molecule on the SrO bilayer.** The hole and its size are indicated. Sr = large blue balls/dots, O = small grey balls/dots, Ti = small red ball/dots.

### Insertion of a TiO<sub>2</sub> molecule into the SrO bilayer with the presence of another TiO<sub>2</sub> molecule

When two TiO<sub>2</sub> molecules absorb on the SrO bilayer, as shown in Fig. S4a, both of the two molecules drag two O from the top SrO layer and form two tetragonal-like TiO<sub>4</sub> molecules, which subsequently induce two O vacancies in the SrO layer. Through a rotation (Fig. S4a) and downward (Fig. S4b) movement, one TiO<sub>4</sub> molecule squeezes a Sr atom out and inserts itself into the top SrO layer.

As shown in Fig. S4c, this  $\text{TiO}_4$  finally has its Ti atom at the original position of the squeezed-out Sr atom, three O (labeled as 2, 3, and 4) close to the O sublattice of the original SrO layer, and one O (labeled as 1) in the new  $\text{TiO}_2$  network (purple dashed square). The squeezed-out Sr becomes an adatom residing above the original SrO layer. The barrier of this insertion process is 1.18 eV, a process taking place at the time scale of  $10^{-7}$  s at  $T = 1023$  K.

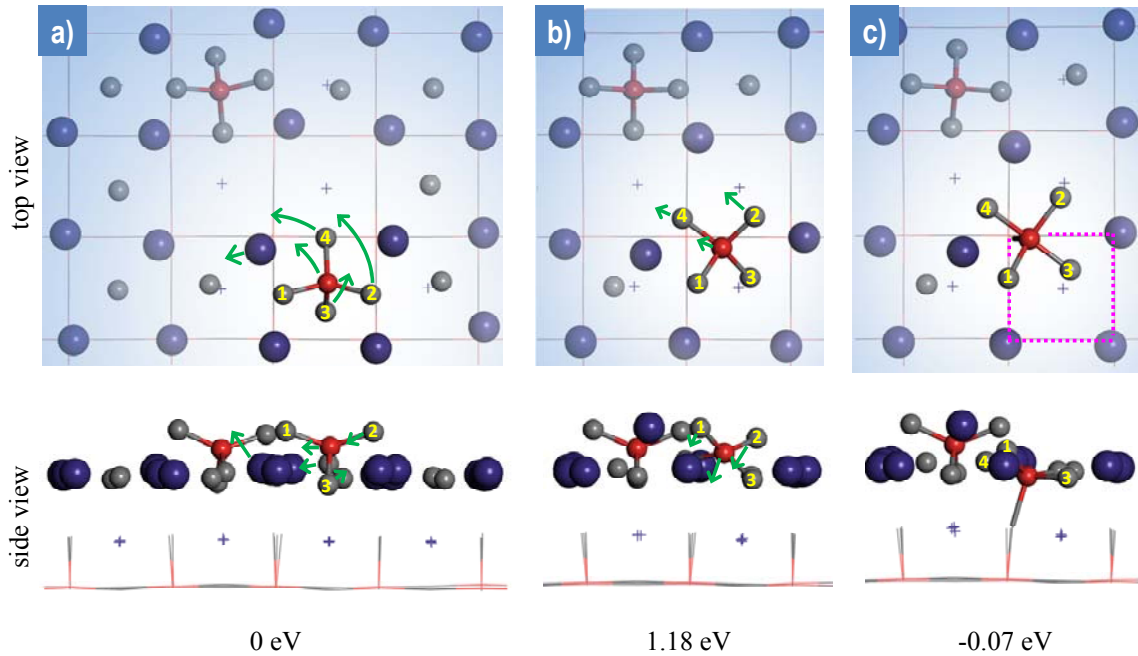


**Figure S4 | Insertion of a  $\text{TiO}_2$  molecule into the SrO bilayer surface with the presence of another  $\text{TiO}_2$  molecule.** **a**, Initial, **b**, transitional, and **c**, final state of this process. The green arrows indicate the atom movements from one state to another. Several atoms are labeled with yellow numbers to guide the eyes. Purple dashed square indicates the  $\text{TiO}_2$  lattice above the bottom SrO layer. Sr = large blue balls/dots, O = small grey balls/dots, Ti = small red balls/dots.

### The modified Buckingham potential and MD simulations

The modified Buckingham potential used in structural optimizations and in MD runs has the form

$$V = A_{ij} \exp\left(-\frac{r_{ij}}{\rho_{ij}}\right) - \left(\frac{c_{ij}}{r_{ij}^6}\right) + \frac{1}{2} \sum_{i=1}^N \sum_{j \neq i=1}^{\infty} \frac{q_i q_j}{r_{ij}}, \quad (1)$$

where  $r_{ij}$  is the distance between atom  $i$  and atom  $j$ . The values of the parameters for strontium titanate (STO) are listed in Table 1.

Table 1. Parameters for the modified Buckingham potential for STO [1]

	$A$ (eV)	$\rho$ (Å)	$c$ (eV·Å <sup>6</sup> )
Sr <sup>1.331</sup> -O <sup>-1.331</sup>	139621.961934	0.1963	2.33222
Ti <sup>2.662</sup> -O <sup>-1.331</sup>	18476.9466310	0.1963	0.00000
O <sup>-1.331</sup> -O <sup>-1.331</sup>	21943.2892770	0.2226	4.14616

The goal of the MD simulations we performed is to shed light on the mechanism of the SrO and TiO<sub>2</sub> layer exchange. The size of the simulation cell in the lateral (x and y) directions, which are replicated using periodic boundary conditions, is 10×10 unit cells of STO. In the z direction (perpendicular to the surface), the simulation cell contains six layers starting with a TiO<sub>2</sub> layer at the bottom and followed by a stacking of SrO-TiO<sub>2</sub>-SrO-SrO-TiO<sub>2</sub>. The two bottom layers were frozen at the equilibrium geometry as obtained in the optimization of the STO lattice. What we were after was how the two upper layers swap to result in an alternating layered structure of STO, which is the energetically most preferred one.

Three different cases were considered. The first corresponds to all perfect layers with no defects. The second represents a situation where vacancy defects are present in the top surface (TiO<sub>2</sub>) layer only. The third is the case when vacancies are present in both the surface TiO<sub>2</sub> and the subsurface SrO layers. The vacancies are created by removing atoms from the optimized zero-temperature structure of the defect-free case. The temperatures we considered ranged from 1000 K to 1800 K in increments of 200 K. At each fixed temperature, the simulation time is 50 ns, with an extra 1 ns added at the start of each simulation to allow for full thermalization.

Our results can be summarized as follows. As expected, increase of temperature results in increasingly more vigorous displacements of the atoms from their

equilibrium positions, but the character of these displacements is different in the three cases explored. At none of the considered temperatures did we observe an interlayer exchange in the time interval of the simulations for the first (defect-free) case. For the second case, however, such exchanges were clearly present starting from the temperature of 1200 K. As shown in Fig. S5, individual Sr atoms migrate from the SrO subsurface layer into and onto the TiO<sub>2</sub> surface layer pulling oxygen atoms from the surface layer with them. The vacancies created in the subsurface SrO layer by the interlayer migration of the Sr atoms are mobile. The situation is similar for the third case, only the extent of the interlayer migration of atoms and the intralayer migration of vacancies is even more extensive. The simulations show that defects could be critical in initiating and sustaining an interlayer migration of atoms that could drive layer swapping for an existing SrO-SrO-TiO<sub>2</sub> stacking. However, these results show only possible first steps in layer swapping and include only the simplest kind of disorder (point defects). Therefore, significant further work is needed to fully characterize the kinetics of layer swapping.

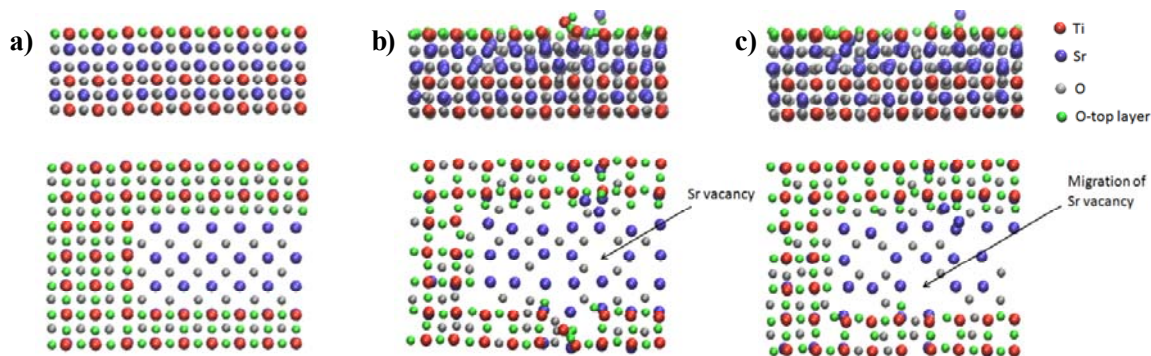


**Figure S5 | Snapshots of MD simulation.** **a**, Zero-temperature structure with an island vacancy in the surface TiO<sub>2</sub> layer (input configuration in the MD simulations). **b**, Structure of the configuration at t=4 ps in an MD run at 1200 K. **c**, The same as **b** but at t=12 ps. See the text for details. Upper: side view; Lower: top view.

### Layer swapping in additional systems

Figure S6 shows that the layer swapping persists in many systems and in different magnetic configurations. For the eight Sr-based systems (B cation X = Ti, V, Mn, Zr, Mo, Ru, Rh, Ir), the swapping from SrSrX to SrXSr and from

SrSrSrX to SrSrXSr are always energetically favorable while that from SrSrXSr to SrXSrSr are unfavorable (Fig. S6a-c), regardless of the magnetic configuration. Similar trends are observed in the La-based systems (B cation X = Cr, Mn, Fe, Co, Ni), expect the cases of LaLaFe and LaLaMn at the Antiferromagnetic/Ferromagnetic (AFM/FM) state. The two stackings at the AFM/FM state are more stable than the LaFeLa and LaMnLa, respectively. However, such abnormality disappears in the NM state, which suggests that this feature comes from the magnetic interactions in the two systems.

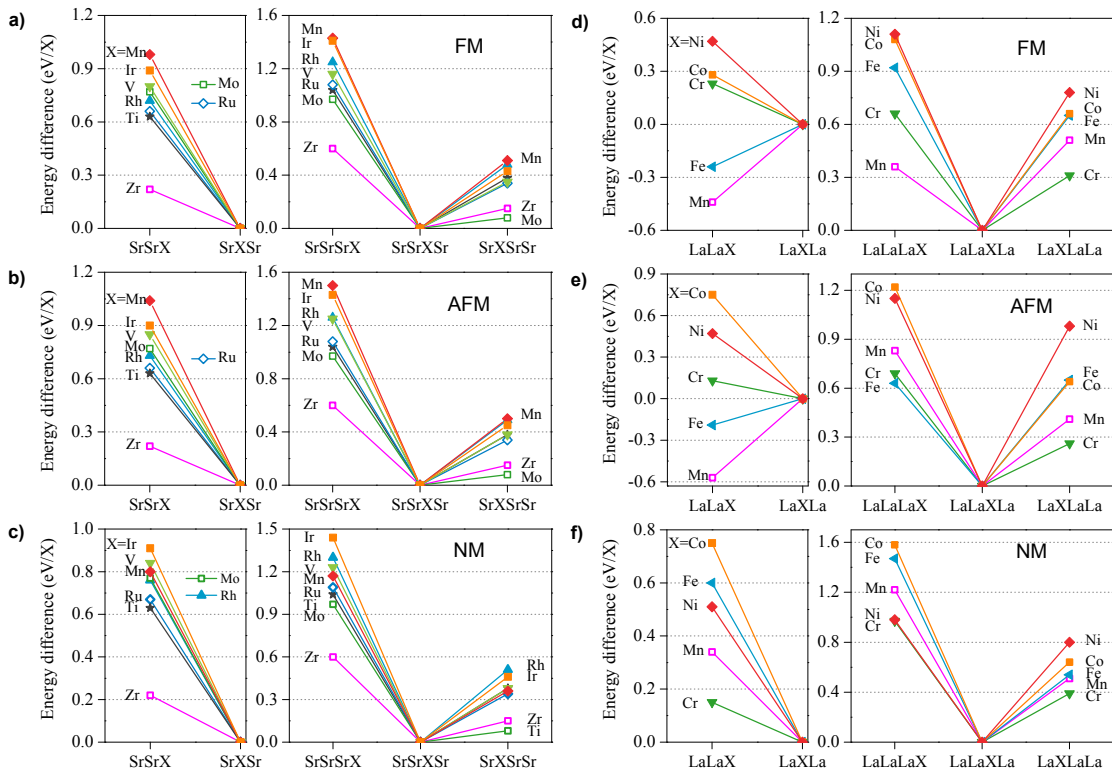


**Figure S6 | Swapping energies in different systems.** a-c, Energy differences among stackings ( $m$ Sr) $X$ ( $n$ Sr) ( $m+n=2$  and 3) at the a, FM, b, AFM, and c, NM states. d-f, Energy differences among stackings ( $m$ La) $X$ ( $n$ La) ( $m+n=2$  and 3) at the d, FM, e, AFM, and f, NM states. The AFM state has the configuration of each spin up (down) X surrounded by four spin down (up) X.

### Theoretical model on the relative energies of the substrate- $m$ SrO- $\text{TiO}_2$ - $n$ SrO stackings

As illustrated in Fig. S7a, by adding a capping structure  $m$ SrO-substrate (A for short) on the top of two stackings, substrate- $(m+n)$ SrO- $\text{TiO}_2$  (B for short) and

substrate- $m$ SrO-TiO<sub>2</sub>- $n$ SrO (C for short), we obtain the same complex, substrate- $(m+n)$ SrO-TiO<sub>2</sub>- $m$ SrO-substrate (D for short). Therefore, the energies have the following relationship

$$\begin{aligned} E_A + E_B &= E_D + CE_{A/B} \\ E_A + E_C &= E_D + CE_{A/C}, \end{aligned} \quad (2)$$

where the  $CE_{A/B}$  and  $CE_{A/C}$  are the energy costs of cleaving D to A and B, and D to A and C, respectively. Simply subtracting these two equations shows that total energy difference  $E_B - E_C$  equals the cleavage energy difference  $CE_{A/B} - CE_{A/C}$ . A careful check shows that the local stacking around the cleavage interface of A/B is TiO<sub>2</sub>/SrOTiO<sub>2</sub> (T/ST for short) at  $m=1$  or TiO<sub>2</sub>/SrOSrO (T/SS for short) at  $m \geq 2$  and that of A/C is SrO/SrO (S/S for short).

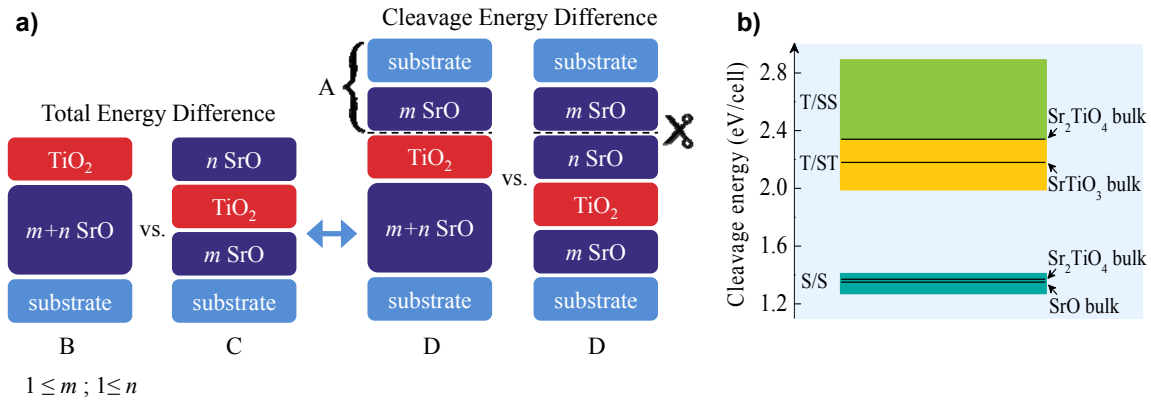


**Figure S7 | Explanation on the driving force of layer swapping.** **a**, Schematics of transforming the total energy difference between substrate- $(m+n)$ SrO-TiO<sub>2</sub> and substrate- $m$ SrO-TiO<sub>2</sub>- $n$ SrO to the cleavage energy difference of substrate- $(m+n)$ SrO-TiO<sub>2</sub>- $m$ SrO-substrate along two different interfaces. The substrate is TiO<sub>2</sub> terminated. **b**, Cleavage energy distribution of the S/S, T/ST, and T/SS interfaces surrounded by thick randomly stacked SrO and TiO<sub>2</sub> layers—except the TiO<sub>2</sub>-TiO<sub>2</sub> stacking—on both sides. The specific values in the SrO, SrTiO<sub>3</sub>, and Sr<sub>2</sub>TiO<sub>4</sub> bulk (with the in-plane lattice lengths fixed to those of the substrate) are indicated by black lines.

Further calculations prove that the cleavage energies of the three interfaces S/S, T/ST, and T/SS depend weakly on the surrounding environment and have the order of  $S/S < T/ST < T/SS$  as seen in Fig. S7b. Therefore, in our model we can replace  $CE_{A/B}$  with the average cleavage energy of T/ST ( $m=1$ ) or T/SS ( $m \geq 2$ ), which are  $\overline{CE_{T/ST}}$  or  $\overline{CE_{T/SS}}$ , respectively, and replace  $CE_{A/C}$  with the average

cleavage energy of S/S, which is  $\overline{CE}_{SS}$ . Consequently, the relative energies of different stackings substrate- $m$ SrO-TiO<sub>2</sub>- $n$ SrO at any fixed  $m+n$  can be calculated using the following formula

$$E_B - E_C \approx \begin{cases} \overline{CE}_{T/ST} - \overline{CE}_{S/S}, & \text{if } m=1 \\ \overline{CE}_{T/SS} - \overline{CE}_{S/S}, & \text{if } m \geq 2 \end{cases} \quad (3)$$

Wherein,  $\overline{CE}_{SS}$ ,  $\overline{CE}_{T/ST}$ , and  $\overline{CE}_{T/SS}$  are, respectively, 1.34, 2.17 and 2.62 eV according to Fig. S7b. We apply the model to the cases in Fig. 3a and obtain good agreement with the DFT results as shown in Fig. S8.

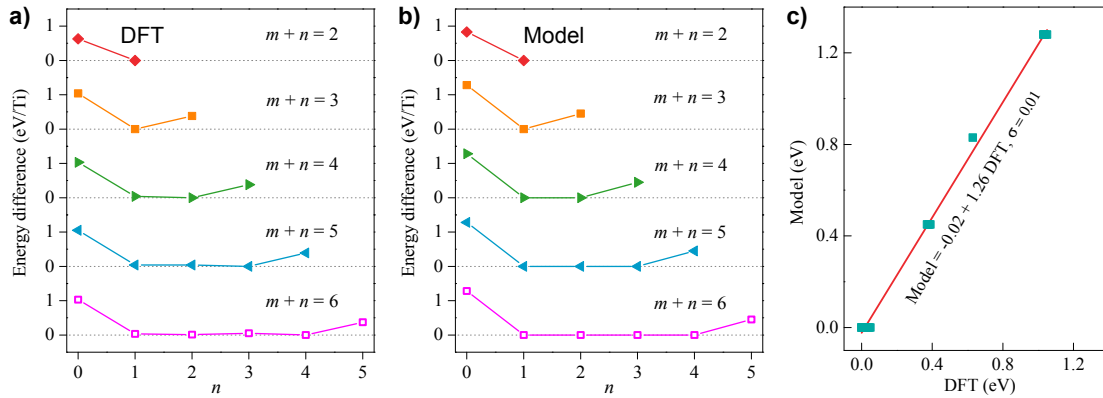


**Figure S8 | Energy differences among substrate-( $m$ SrO)-TiO<sub>2</sub>-( $n$ SrO) for  $m + n = 2, 3, 4, 5, 6$ .** Results from **a**, DFT calculations and **b**, our model based on the average cleavage energies of the S/S, T/ST, and T/SS interfaces. **c**, Direct comparison between the DFT and model results.

## References

1. Sekiguchi, S. *et al.* Atomic force microscopic observation of SrTiO<sub>3</sub> polar surface. *Solid State Ionics* **108**, 73–79 (1998).